Preferred citation: U. Hirn, J. Kritzinger, M. Donoser and W. Bauer. Introducing a concept to link 3D paper structure to 2D paper properties. In **Advances in Pulp and Paper Research, Oxford 2009**, *Trans. of the XIVth Fund. Res. Symp. Oxford, 2009*, (S.J. I'Anson, ed.), pp 721–747, FRC, Manchester, 2018. DOI: 10.15376/frc.2009.2.721.

INTRODUCING A CONCEPT TO LINK 3D PAPER STRUCTURE TO 2D PAPER PROPERTIES

Ulrich Hirn[1], Johannes Kritzinger[1], Michael Donoser[2] and Wolfgang Bauer†

[1]Institute for Pulp-, Paper- and Fiber Technology
[2]Institute for Computer Graphics and Vision,
Graz University of Technology, Austria

ABSTRACT

This paper introduces a concept that spatially links local paper properties from a 3D paper dataset to a 2D paper property map of the same sample. The concept exploits the fact that paper is a planar structure. This permits successive conversion of 3D paper datasets first to a 3D surface (the paper center surface) and further to a plane. The flattened 3D paper data can then be linked to the 2D paper property map. Laser micro holes applied to the paper are employed as marks for alignment of the 2D maps. The key step of the procedure is flattening the paper data from a warped 3D surface to a 2D plane.

Some exemplary applications for the introduced method are given. The effect of local coating layer thickness on local brightness and local print density is examined for wood free coated paper. Furthermore, the concept can be applied for quantitative comparison of data from different 3D-imaging techniques. We measured local coating layer thickness on the same paper specimen applying first fan-beam X-ray microtomography and then microtome serial sectioning. The results are compared using point-wise correlation.

1 INTRODUCTION

Research on paper structure and its effect on paper properties has increasingly focused on measurement methods that evaluate local paper properties, i.e. methods that deliver 2D paper property maps. Such methods inherently address the inhomogeneity of paper and thus provide better insight in its behavior. A common approach is to *register*, i.e. to spatially align, paper property maps showing the same region of a paper sample. These aligned maps enable qualitative analysis by visual inspection but also quantitative analysis of interrelations between local paper properties, e.g. by point-wise correlation.

In the field of printability research it is common to link images of the printed paper to maps of local paper properties in order to find the reasons for missing ink transfer or local variations of print density (print mottle). Local print density variations have been registered with maps of local basis weight (beta formation) and surface topography [1, 2, 3] or coating thickness and latex concentration [4]. Regions with missing ink have been linked to maps of surface topography [5] and formation [6]. Finally, offset fiber picking has been analyzed with aligned maps of print and formation [7].

Registered paper property maps have also been used to investigate fundamental paper properties. Local apparent density has been studied regarding calendering and hygroexpansivity [8] and z-directional compressibility [9]. The connection between local basepaper thickness and the associated local coating layer thickness [10, 11], interrelations between local gloss and topography [12] as well as paper surface topography changes under load [13] have been investigated. The spatial interrelation between basis weight and fiber orientation [14] has also been analyzed.

The rapid development in the field of 3D micro-imaging techniques has also promoted paper structure research. Most of the work in this field has been devoted to X-ray microtomography. The highest quality is achieved in a synchrotron tomograph, where the X-rays in the beam are monochromatic and parallel. Synchrotron tomography can be performed either in absorption mode [15] or in phase contrast mode [16]. Fan-Beam X-ray microtomography, e.g. [17], achieves images of lower quality, however this technology is less costly than synchrotron tomography and it is developing fast. Other important applications for 3D imaging of paper are Confocal Laser Scanning Microscopy [13], optical coherence tomography [18] and microtome serial sectioning in combination with light microscopy [19].

From 3D-imaging techniques additional *local* information about the paper structure can be extracted. Most notably local void volume and local pore size [20] can be determined. Also local coating layer thickness [19] or local printing ink penetration [21] is measured. Initial work to extract filler particles [15] and fiber morphological parameters to detect e.g. softwood and hardwood fibers [22] has been published.

It seems promising to link the results from 3D- and 2D paper imaging techniques. Inhomogeneities in print have e.g. been analyzed qualitatively by comparing results from 2D imaging techniques with 3D-reconstructions of paper structure [23, 24].

In our paper we will introduce a concept that spatially links *local paper properties extracted from 3D-imaging* to *2D paper property maps*. Such joint datasets combine results from the fast developing 3D-paper structure analysis with the well established 2D-measurement methods. This permits new approaches to analyze paper structure and its interrelation to paper properties. After describing an implementation for our concept (section 2) we present a qualitative validation of the method and initial applications (section 3). We investigate the interrelation between local coating coverage and local paper brightness as well as print reflectance. Finally, we demonstrate, that the proposed concept can be used for quantitative comparison of 3D paper datasets. We compare coating layer thickness measurements on the same paper sample using fan beam X-ray microtomography and light microscopy based serial sectioning.

2 LINKING 3D AND 2D PAPER STRUCTURE

Our concept exploits the fact that paper is a planar structure. This permits successive conversion of 3D local paper property data first to a 3D surface (the paper center surface) and further to a plane, Figure 1. From a 3D dataset of paper, as symbolized in Figure 1(a), we first extract some local features, e.g. coating layer thickness on the paper top side, 1(b). The results of the feature extraction are locally evaluated and assigned to the according position on the paper center surface, Figure 1(c). The crucial step of the whole process is flattening of the center surface and the associated local paper property values, symbolized in Figure 1(d). The round holes in the paper sample in Figure 1 are marks that have been applied to register the flattened paper property map to other measurement maps. The concept consists of the following four steps, they will be described in detail in the following sections.

1. Applying marks to the paper which can be used for aligning of the resulting 2D maps, section 2.1.
2. Measuring local paper properties in the 3D dataset and assigning the results to the according position on the paper center surface, section 2.2.

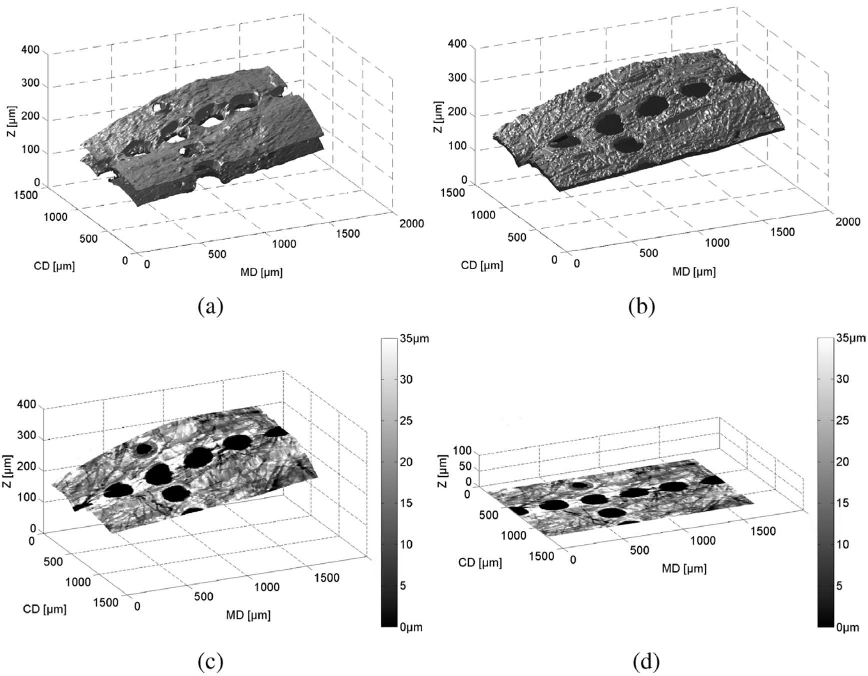

Figure 1. Extraction of 2D paper property maps from 3D paper structure. A wood free coated paper sample has been marked with micro holes and imaged in an X-ray microtomograph (a). Coating layer thickness at the top side of the sample is extracted (b). The local coating thickness values are assigned to the paper center surface (c). The surface and the according data values are flattened (d).

3. Flattening of the center surface and the associated data, section 2.3.
4. Registering the resulting 2D paper property map to some other 2D map using the marks applied in step 1, section 2.4.

2.1 Lasermarking

Marks are applied to the paper to indicate defined positions on the specimen. These marks are necessary to align the final 2D paper property maps, section 2.4. For registration of paper property maps often hole marks are used [1, 2, 7], sometimes a mark is placed on the paper e.g. a piece of adhesive tape [25]. The holes should be as small as possible to be able to apply them to high resolution datasets. Initial trials using pinholes did not prove successful, the holes had a diameter of 0.5 mm and the surrounding paper structure was deformed severely within 1 mm diameter. Very small holes in paper can be realized using pulsed lasers e.g. for perforation in packaging [26] or for document security [27], also cigarette papers are often laser perforated [28, 29]. For cutting and perforating of paper usually CO_2 lasers are recommended [30] because all organic materials have strong infrared light absorption at 10.6μm, which is the preferred operational wavelength of CO_2 lasers.

For application of mark holes we use a pulsed 100W Synrad CO_2 laser with fixed focus. The material is removed by direct evaporation and burning due to the laser beam. The laser is air assisted to blow out the evaporated material. Laser pulse width is 0.005s with a pause of 0.1s between pulses. The laser is mounted on a two axis PC-controlled stage. Simultaneous control of the stage movement and the laser permits application of a defined mark pattern on a paper specimen. A line pattern like in Figure 2(b) is well suited for registration of 2D paper property maps [25].

The described method works on a wide range of grammage and paper grades, from 50 g/m^2 SC-paper to 200 g/m^2 wood free coated paper, Figure 2(a). Depending on the paper basis weight the holes have a diameter from 150–200μm. Although a small region around the hole is burnt by the laser, compare Figure 6, the holes have sufficiently regular geometry and sharp bounds to be used for image registration.

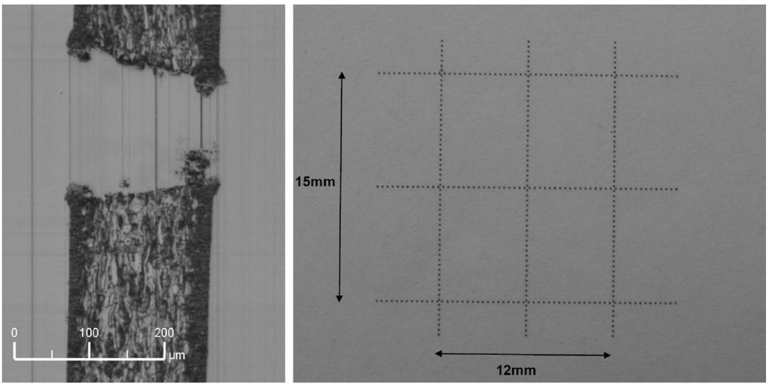

(a) (b)

Figure 2. Microscope image of a laser hole in a 200 g/m^2 wood free coated paper (a). Using a PC-controlled laser and a 2-axis moveable stage it is possible to generate a defined hole pattern (b) for registration of paper property maps.

2.2 Assigning locally measured paper properties to the center surface

The second step of converting a 3D paper dataset to a 2D paper property map is measuring the desired paper property in the 3D dataset and projecting its local value to the paper center surface, Figure 1(b,c). The principle is outlined on measurement of coating layer thickness, Figure 3. However it must be noted that this method [19] can be applied to all types of measurements in 3D paper datasets, e.g. surface topography, local pore diameter etc.

The top image of Figure 3 shows a slice of a wood free coated paper digitized with microtome serial sectioning and light microscopy. The coating layer of the paper is identified image analytically (middle image). The slice center line is calculated as a smoothed mean of the paper surface lines. Coating layer thickness is extracted along equally spaced measurement lines perpendicular to the center line. Local paper property values are extracted from every slice image and assigned to its center line. The center lines of all slices with their associated local paper property data define the paper center surface.

2.3 Flattening of the warped center surface

The key processing step in the proposed concept is converting the curved 3D surface to a flat plane. This is the classic geometry problem of *developing* a surface. A developable surface can be flattened, i.e. transformed to a plane, without being stretched or torn. In many fields of science it is necessary to find a mesh of planar elements that approximates a defined surface e.g. in computer graphics or mechanical engineering. The multitude of existing

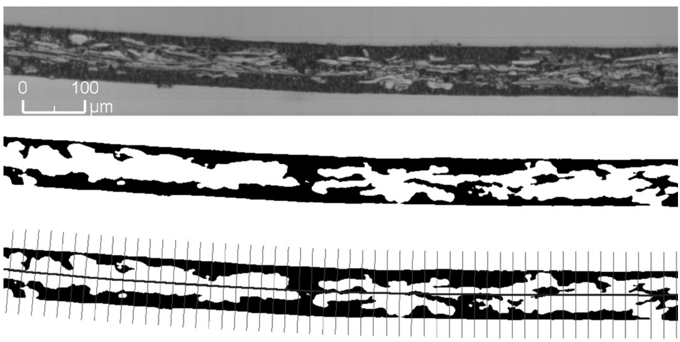

Figure 3. The coating layer of a wood free coated paper (top) is detected using image analysis (middle). The local coating layer thickness values are extracted along measurement lines that are perpendicular to the paper center line [19].

developing algorithms however is not applicable to our problem because they find an optimal mesh for an algebraically defined surface. We want to find an optimal development of an *existing discrete mesh*, i.e. our center surface of the paper.

Development of a given mesh is e.g. applied in textile engineering or image processing [31, 32, 33, 34, 35]. The key idea of all these methods is to build a *physical model* of the surface as a 3D mesh of vertices (nodes) connected by springs. This physical model is manipulated by applying external forces to the mesh and using the physical laws of mechanics to model the reaction of the mesh.

In our approach flattening is achieved in two steps, Figure 4. First the original length of the springs in the 3D mesh is calculated. Then the nodes are vertically projected to the xy- plane, the springs that are non-parallel to the projection plane are thereby compressed. Subsequently the springs are relaxed by moving the vertices within the xy- plane. During relaxation the model converges towards a state of minimal overall spring energy which is considered as the optimal solution of the flattening problem, the dashed grey lines in Figure 4.

In the following section we describe our implementation of the method in

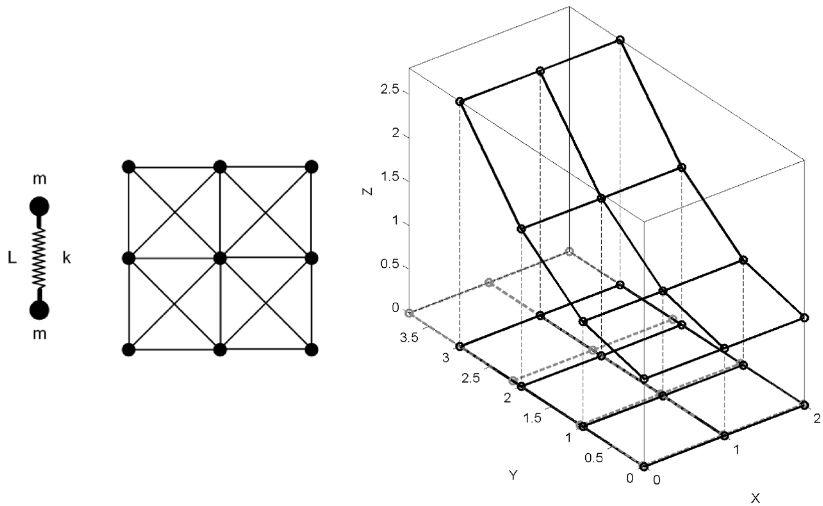

Figure 4. Each vertex of the mesh is connected to its eight neighbours by a spring (left). For flattening (right) the 3D mesh (black) is first projected to the xy-plane. Compressed springs expand in the xy-plane and the mesh relaxes. The relaxed mesh (dashed grey lines) is the final 2D development of the 3D mesh.

detail and discuss the literature, finally the accuracy of the algorithm is verified using test models.

2.3.1 A mechanical model for flattening of a discrete 3D surface

Although most of the flattening procedures for discretized 3D surfaces are based on triangular meshes [31, 32, 34, 35], only few [32] are restricted to that condition. For two reasons we have chosen a quadrangular [33] mesh. First our paper center surface data is given as a quadrangular mesh, second this structure permits analysis of the deformation type (shear or axial deformation). Every vertex in the mesh is connected to its neighbours with 8 springs, Figure 4 (left). All springs respond to axial deformation, the diagonal springs are necessary to correct shear deformation parallel to the non diagonal springs' axes.

The key idea of our flattening approach is illustrated in Figure 4 (right). We start with a 3D mesh that is equally spaced in x and y direction. In the fist step the original length L of the springs is recorded, at this point the springs are relaxed. The length of the springs depends on the gradient of the surface, a spring on a steep edge is longer than one parallel to the xy plane. Then the vertices (black) are projected to the xy plane. The springs of the 3D surface are thereby compressed to length l, the degree of compression depends on the magnitude of the local surface gradient $|\nabla f(x, y)|$. For mesh relaxation the vertices are only allowed to move within the xy plane. The springs start to re-expand to their original length L. If the 3D surface is developable they will eventually reach their original length, the dashed grey mesh in Figure 4 (right). If not the mesh will converge towards an equilibrium state at minimum spring energy.

2.3.2 Relaxing the spring connected mesh

For relaxation of the mesh in the xy-plane different approaches are used. Some [31, 32, 35] perform direct minimization of the cumulative spring energy

$$E = \sum k(l_i - L_i)^2. \tag{1}$$

where L_i denotes original spring length in the 3D mesh and l_i is current spring length of spring i. Others assign a mass m to each node and model the dynamic behavior of a dampened mass-spring system [33, 34]. They apply Newton's second law $F = m \cdot a$ where m is a mass, F is a force acting on the mass and a is the resulting acceleration. We also use this approach. In vector notation we write position of node i as $\boldsymbol{x}_i = [x,y,z]^T$ and velocity $\boldsymbol{v}_i = [v_x\ v_y\ v_z]^T$. We model the spring force according to Hooke's law as $(l - L)k$, where k is the spring constant. We denote the vector of spring from node $\boldsymbol{x_i}$ to node $\boldsymbol{x_j}$ as $\boldsymbol{x_{ij}}$ and the initial length L of a spring between neighbouring nodes i and j as L_{ij}. The cumulative spring force $\boldsymbol{F_i}$ acting on node i is found as the sum of spring forces imposed from the eight neighbouring nodes j

$$\boldsymbol{F_i} = \sum_{j=1}^{8} \boldsymbol{x_{ij}} \frac{(L_{ij} - |\boldsymbol{x_{ij}}|)k}{|\boldsymbol{x_{ij}}|}. \tag{2}$$

Our model furthermore contains a velocity proportional dampening force $-\boldsymbol{v}c$ for gradual dissipation of the system energy, c is called dampening constant. Acceleration being the second derivative $\ddot{\boldsymbol{x}}$ and velocity the first derivative $\dot{\boldsymbol{x}}$ of the position we can rewrite Newton's second law for a vertex i as

$$m\ddot{\boldsymbol{x}}_{\boldsymbol{i}} = \boldsymbol{F_i} - c\dot{\boldsymbol{x}}_{\boldsymbol{i}}. \tag{3}$$

Movement of the mesh vertices during relaxation is found by coupling the vertices via the spring forces. The movement of the vertices over time, i.e. the relaxation of the mesh, is found by solving Equation (3) for *every vertex i*. The obvious solution would be discrete integration along timesteps Δt where $\dot{x}(t + \Delta t) = \ddot{x}(t)\Delta t$ and $x(t + \Delta t) = \dot{x}(t)\Delta t$. This method, Euler Integration, however is numerically instable. Other implementations [33, 34] of relaxing a spring connected mesh therefore use Runge-Kutta integration or Verlet integration. We implemented second order Runge-Kutta integration [36]. For our implementation we set vertex mass $m = 1$ and spring constant $k = 1$, all the constants as well as the variable t have unit 1 because they do not reflect physical units.

Solving timestep integrals can be accelerated by several orders of magnitude using adaptive control of timestep size Δt. However numerical stability of the integration must be preserved. For performance reasons we have not implemented detection of node collision or nodes crossing a spring, both events lead to immediate collapse of the model. Therefore we need careful control of timestep size. We developed an approach that simultaneously controls the dampening coefficient c and Δt. Initially the spring tensions are very unevenly distributed on a micro scale, i.e. we have a high local gradient of node forces $|\nabla \boldsymbol{F_i}(x, y)|$. This leads to chaotic movement of the nodes which makes it necessary to start the iteration with very small timesteps. Additionally we reduce this chaotic movement by starting integration with high values for the dampening coefficient c. As the small scale tensions even out, chaotic movement decreases and correction of large scale mesh deformation becomes dominant. This results in a more aligned movement of the vertices which shows in a decrease of node velocity gradients. More aligned node movement reduces the risk of vertex collision, it is possible to increase timestep size Δt and decrease dampening coefficient c for faster convergence. We control Δt as well as c depending on the maximum velocity gradient in the mesh $max(|\nabla \boldsymbol{v_i}(x,y)|)$. The controlling conditions for timestep size Δt and dampening coefficient c are

$$\Delta t < \Delta t_{max} \quad \text{and} \quad max(|\nabla \boldsymbol{v_i}(x,y)|) < a \tag{4}$$

$$c > c_{min} \quad \text{and} \quad max(|\nabla \boldsymbol{v_i}(x,y)|) < b \cdot c. \tag{5}$$

We run the model with the following values for the constants: $a = 10^{-2}$, $b = 0.2$, $\Delta t_{max} = 0.3$ and $c_{min} = 0.02$. Furthermore the maximum distance a node is allowed to move within a timestep is limited to 20% of initial grid spacing in the xy plane, otherwise Δt is reduced accordingly. Controlling the parameters Δt and c using Equations (4) and (5) reduces runtime of the mesh flattening by factor 300. Relaxing a mesh of 128 × 96 nodes takes 35s on a 2GHz desktop PC using adaptive control of Δt and c, for fixed parameter integration it takes 1 hour and two minutes.

2.3.3 Termination and accuracy of mesh relaxation

During the relaxation process system energy is gradually dissipated by the dampening term in Equation (3). The dampening constant c must be chosen such to obtain an underdampened system [37] because runtime explodes when c is above critical dampening. An underdampened system oscillates around its equilibrium (i.e. the state of maximum relaxation). That makes it necessary to define a termination criterion which ensures a defined accuracy of the result.

In order to measure accuracy of the results, test datasets were generated. We constructed an equally spaced mesh, i.e. vertex distance was set to 1 in x- and y- direction, Figure 5(a). Spring length was recorded, then the mesh was subjected to various deformations as the may appear in a center plane of a 3D dataset. We applied axial and shear deformation as well as random displacement of individual nodes and entire rows, Figure 5(b). Relaxation of the mesh using the described method restores the original geometry, Figure 5(c). The error of the relaxation is measured from the difference in geometry between original and restored mesh. We measured differences of width,

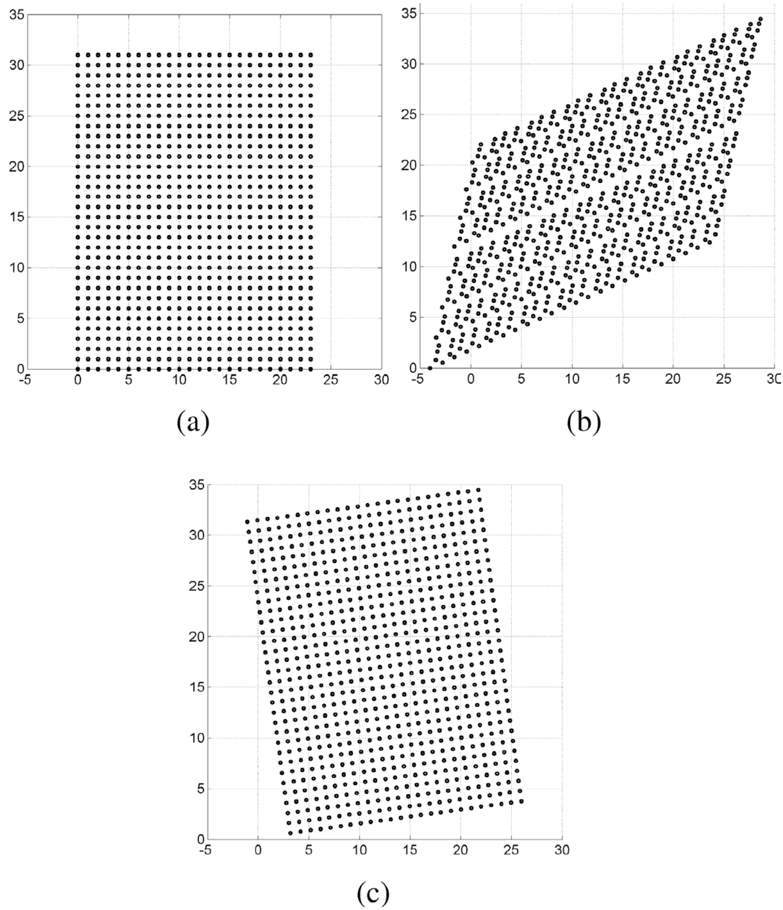

Figure 5. Test dataset of an equally spaced mesh having 32 × 24 vertices (a). The mesh is deformed using shear, rescaling, row-wise displacement and random displacement of individual nodes (b). Relaxing the mesh as described in section 2.3.2 fully restores the original geometry (c). Geometric error of the restoration was below 0.01%, runtime was 4s on a 2GHz desktop PC.

height and aspect ratio. Geometric error of the restored mesh in Figure 5(c) was below 0.01%.

It might be intuitive to use a termination criterion based on spring energy in the system. This however is not applicable for our problem. Non developable surfaces reach system equilibrium at a spring energy greater zero, it is impossible to tell in advance how large this value will be. Instead we chose the average value of node speed $|\boldsymbol{v}_i|$ as termination criterion

$$\frac{1}{i}\sum|\boldsymbol{v_i}| < 10^{-3}. \tag{6}$$

Using the termination criterion from Equation (6) in a series of test cases, geometric error of the restored mesh was always below 0.1%. Recent experiences relaxing large meshes however suggest that other criteria might be a better indicator for termination. Still the test cases demonstrated in this section prove, that the mesh relaxation algorithm works correctly.

2.3.4 Mapping the data from the 3D to the 2D mesh

Finally the paper property data, e.g. visualized as a coating layer thickness image in Figure 1(c,d), is mapped from the 3D to the flattened 2D mesh. This is accomplished by interpolation of the image data. The image data *values* remain the same as in the 3D surface, only their *position* has changed during flattening. Interpolation of this type of data is not trivial, because the data points are not regularly spaced after mesh relaxation. They are interpolated to an evenly spaced form, i.e. the final output image of the flattened data. We use a standard algorithm implemented in MATLAB. It is based on Delaunay triangulation [38] of the unevenly spaced data points and subsequent bilinear interpolation within these triangles to find resampled, evenly spaced image data.

2.4 Registration of 2D paper property maps

Registration aligns two different 2D property maps of the same paper specimen. In the combined dataset the data of both measurements are available for each spatial location on the paper. A flattened 3D dataset can be registered to any other 2D property map of the same paper specimen. Figure 6 shows registered images of local coating layer thickness and local paper brightness of a WFC paper.

Standard concepts of image registration [39, 40, 41] have been implemented to accomplish this task. For registration of our paper property maps we assume a *rigid deformation* of the image data. That means that the images are translated, rotated and rescaled for matching. Translation and rotation correct different fields of view in the images, rescaling enables registration of images with different pixel size. For the matching process control points in the laser mark holes are manually selected in both images. From the control

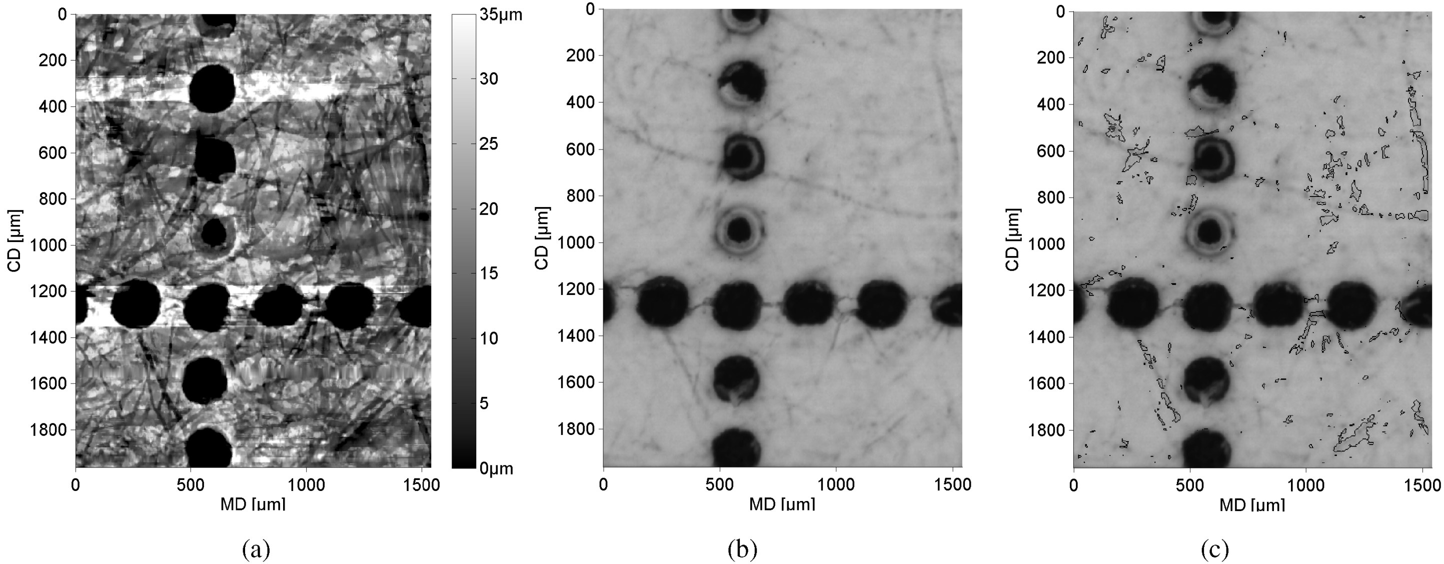

Figure 6. Mapping the coating thickness values of a WFC paper sample (a) to the according diffuse illumination microscopy image (b). The images show exactly the same region of the paper. Regions with less than $5\mu m$ coating thickness are outlined in (c). The outlined low coat weight regions are congruent with the darker regions of the microscope image, the registration of the datasets is correct.

points the *rigid image transform matrix* is calculated using least square minimization of the transformation error between the two sets of control points. Finally, the image pixel coordinates are warped using the previously calculated transform matrix and the registered image is calculated using bilinear interpolation.

An extensive discussion of different registration methods for paper property maps, a detailed mathematical description of our registration method and an evaluation of its accuracy has been published earlier [25].

3 RESULTS

This section first gives a qualitative example that the proposed method to link 3D and 2D paper properties works sufficiently accurate. Then some exemplary applications are outlined. The effect of local coating layer thickness on local brightness and local print density is examined for wood free coated paper. Finally, the concept is applied for quantitative comparison of coating layer measurement using two different 3D imaging methods: serial sectioning combined with light microscopy and fan-beam X-ray microtomography.

3.1 Materials and measurements

The samples examined in the following sections are wood free coated (WFC) papers with a basis weight of 90 g/m^2, 118 g/m^2 and 135 g/m^2. The optical images of the printed and unprinted paper surface were acquired using an optical microscope [42] equipped with diffuse illumination under 2.5 × magnification. Laser marks have been applied using the technique described in section 2.1.

3-dimensional datasets of paper samples were acquired using two techniques. Serial sectioning combined with light microscopy [19] is a fairly new 3D micro imaging method for paper. A paper sample is embedded in resin and serial sectioned in a microtome with slices of a thickness of 3–9μm. After each cut the paper is imaged using a microscope mounted on a 3-axis scanning stage. Serial cutting and imaging of the paper sample is fully automated. We chose a resolution of $3 \times 3.24 \mu m^2$ in the paper plane and $0.81 \mu m$ in z-direction. Samples were also analyzed using a SkyScan 1172 X-ray microtomograph [17]. The according datasets had a voxel size of $1.37 \times 1.37 \times 1.37 \mu m^3$.

3.2 Registration accuracy

In section 2.3.3 it has been shown that the relaxation of the spring connected mesh works accurately. The geometry of a deformed mesh has been recovered with a residual error below 0.1%. Now we want to demonstrate *overall* accuracy of all four processing steps of the concept. During these steps several possible sources of error may occur. During 3D imaging microtomography as well as microtome serial sectioning produce discontinuities and skewed sample regions. Also the quality of the calculated paper center plane heavily depends on the image analysis methods applied. Finally, registration of the flattened 3D data to the 2D map might introduce errors.

The overall accuracy of all processing steps is illustrated qualitatively in Figure 6. All images in the figure show exactly the same region of the paper, the coordinate systems in 6(a, b, c) are congruent. According to Kubelka-Munk theory a declining impact of coat weight on brightness has to be expected. Thus only regions with a *very* thin coating layer are expected to exhibit visibly lower local brightness. All regions with less than $5\mu m$ coating thickness are outlined in Figure 6(c). If the combination between the 3D coating layer data and the 2D paper surface image has worked correctly it is to be expected that the outlined low-coatweight regions are positioned on the darker areas of the surface image. Indeed these regions and regions of reduced brightness are congruent to a large extent, visual inspection of Figure 6(c) shows only minor displacements in the size range of $10–20\mu m$. This suggests, at least in a qualitative sense, that the described implementation of linking 3D paper structure data to 2D paper property maps works satisfactorily.

3.3 The effect of coating layer thickness on brightness variation and print unevenness

Uneven or missing coating coverage leads to whiteness mottle of the paper and print unevenness, especially in the middle tones of printing. As exemplary applications for linking 3D paper structural information to 2D paper property maps we present an initial investigation of the interrelation between coating layer thickness on the one hand and local brightness variations and print density variations on the other.

3.3.1 The effect of coating layer thickness and calendering on brightness variations

The effect of insufficient coating coverage on a small scale is visible in Figure 6. Small structures, most prominently individual fibers, shine through the coating. While these small details may be interesting from a scientific point of view, they can not be observed by the end user of the paper. Larger areas have to be considered at a coarser resolution to analyze structures visible with the naked eye.

We studied two samples of an industrial 135 g/m^2 WFC paper, one before and one after calendering. Calendering reduces opacity and brightness, also local brightness variations increase considerably, Figure 7(a, c). The paper has been laser marked, coating layer thickness has been measured and linked to the optical image of the paper surface, Figure 7(b, d). Visual inspection shows that, similar to Figure 6, many of the elongated grey structures can immediately be attributed to fibers with insufficient coating coverage. Also some larger scale structures exhibit the expected relation between higher coat weight and higher brightness, e.g. the high coat weight region at $x = 6mm$ and $y = 2.5$–$3mm$ in the uncalendered paper (a, b). However for some of the inhomogeneities in the optical image no corresponding coating layer variation can be found.

Quantitative analysis of the relationship between local brightness, i.e. reflectance of the paper surface, and coating layer thickness is shown in Figure 8. The plot is drawn from the data in Figure 7, which has been rescaled to a pixel size of $100 \times 100\mu m^2$. This is approximately the structure size that can be resolved by the human eye under excellent illumination and a viewing distance of $30cm$. The region of the laser holes has been excluded for the scatter plot. The linear correlation coefficients are not high, $r^2 = 0.26$ for the uncalendered and $r^2 = 0.21$ for the calendered paper, still there is an evident trend.

The observed relationship between local brightness and coating layer thickness differed from expectations in two ways. First the correlation is lower than expected, second the interrelation was expected to exhibit a more pronounced saturation towards higher coating thickness values. For the uncalendered paper the relation is hardly saturating, the calendered paper shows more saturation. Analyzing these results with the Kubelka-Munk equations for mono- and multi-layer structures [43] could provide further insights.

Regarding the rather low correlation between coating thickness and optical reflectance there are two aspects. First the differences between the uncalendered and calendered sample are discussed, second possible reasons for the low correlation are given. During calendering the basepaper caliper decreases from $59.5 \pm 0.4\mu m$ to $50.5 \pm 0.4\mu m$ and the coating layer thickness decreases from $17.4 \pm 0.2\mu m$ to $16.6 \pm 0.2\mu m$. Still the pore volume for WFC paper, measured with mercury intrusion, usually decreases 30% to 50% [44]. It can be assumed, that the compression during calendering leads to uneven densification of basepaper and coating. Thus it could be expected, that the

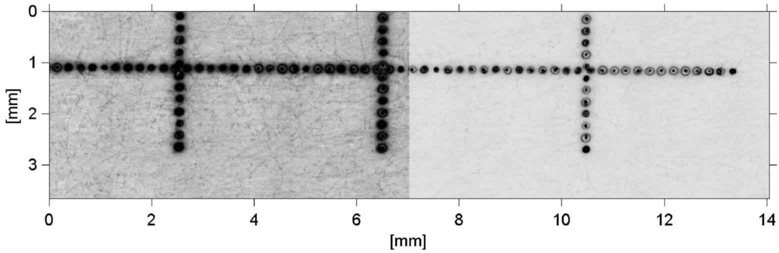

(a) Local brightness, uncalendered paper.

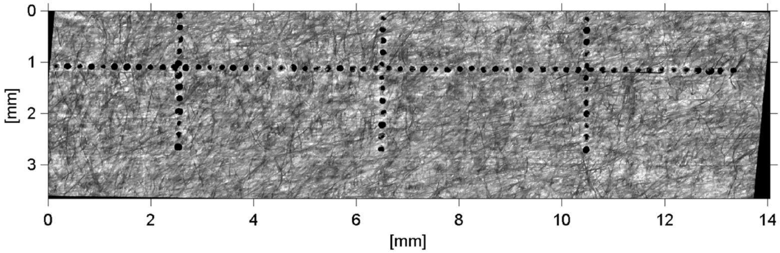

(b) Coating layer thickness of (a).

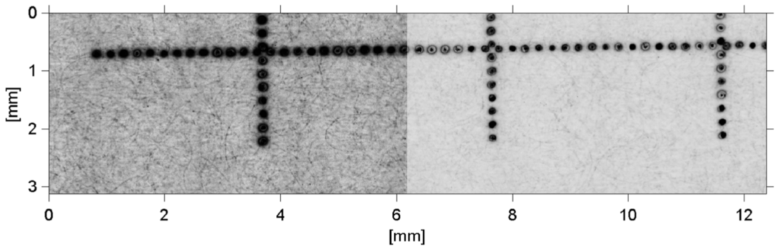

(c) Local brightness, calendered paper.

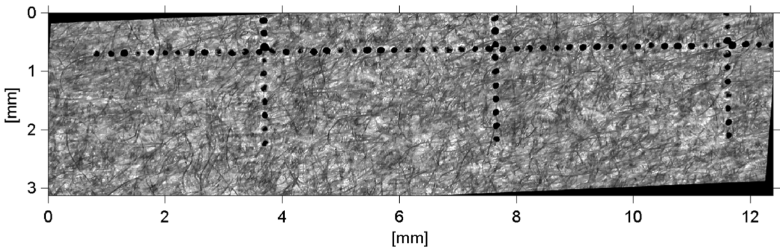

(d) Coating layer thickness of (c)

Figure 7. Local brightness (a, c) and local coating thickness (b, d) of a WFC paper before (top a, b) and after (bottom c, d) calendering. The left half of the local brightness images is contrast enhanced. Pixel size is $12 \times 12 \mu m^2$, values in the coating thickness maps vary from 0 g/m^2 (black) to 35g/m^2 (white).

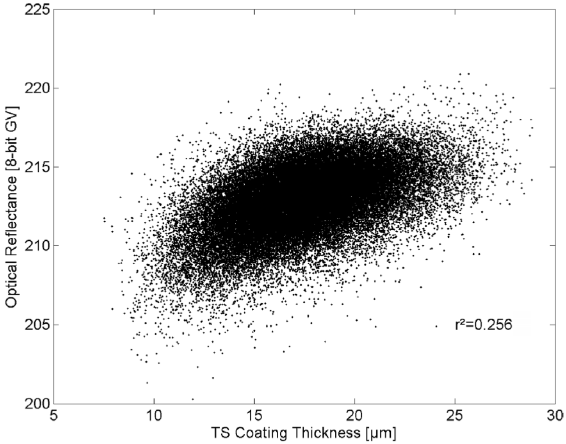

(a)

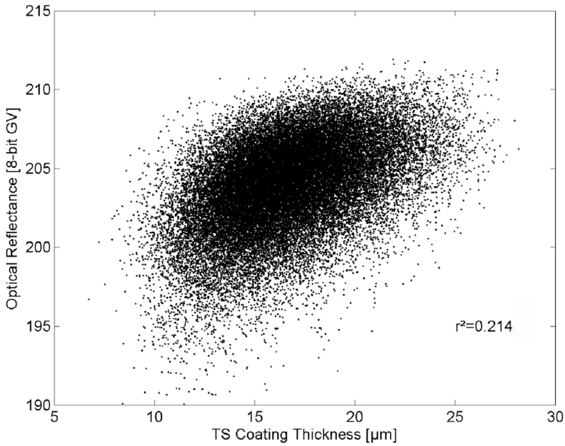

(b)

Figure 8. Point-wise linear correlation between coating layer thickness and local paper brightness at a point size of $100\mu m$. The scatter plots refer to the WFC paper in Figure 7, uncalendered (a) and calendered (b).

interrelationship between optical reflectance and coating layer thickness is weaker after calendering. The correlation is indeed a little lower for the calendered sample, $r^2 = 0.26$ vs. $r^2 = 0.21$, however this difference is small. There are several possible reasons for the low correlation between local brightness and coating thickness.

- First of all the data flattening and registration procedure introduces some error. The regions with locally lower brightness are small, thus even small misalignment between the maps decreases the correlation.
- Other sources of error are measurement of the optical reflectance and coating layer thickness. The illumination of the reflectance measurement is not entirely diffusive, thus some brightness variations in the image descend from topography variations. This is particularly the case for the uncalendered paper. Also the image analytical segmentation and measurement of coating layer thickness introduces some error.
- Variations of local base paper opacity and reflectance are not considered in the analysis. Local variations in filler content, fiber type and basepaper density can have a large effect on local optical reflectance.
- Finally our analysis neglects opacity variations within the coating layer.
  – The investigated paper is triple coated, the base coating usually has a lower opacity than the top coatings. This is not accounted for in the analysis.
  – There are local variations in coating composition and coating density. These factors lead to opacity variations in the coating, there is evidence that these variations have been observed with Raman spectroscopy [45].

In conclusion the reasons for the weak interrelation between local brightness and coating layer thickness can not be explained within the scope of this paper, further examinations according to the points discussed above will bring interesting insights.

3.3.2 Coating layer thickness and print density variations

Another exemplary application investigates the effect of local coating layer thickness on local print reflectance. A 118 g/m^2 WFC paper printed in an industrial sheet fed offset printing press has been analyzed. The sample was extracted from the 40% black tone value field where the print showed considerable raster mottle. It was laser marked and digitized to a 3D dataset using microtome serial sectioning. Again coating layer thickness was measured and the flattened data was registered to a high resolution image of the paper surface, Figure 9.

Visual inspection of Figures 9(a, b) already indicates that regions with less coat weight also have less print reflectance, they look darker. In order to enable point-wise correlation the printing dot pattern was removed by low-pass filtering with a symmetric Gaussian kernel having a size of $6\sigma = 420\mu m$. The coating layer was also smoothed using the same kernel, Figures 9(c, d). The smoothed data was rescaled to a pixel size of $100\mu m$ and point-wise correlation of print reflectance and coating layer thickness was performed,

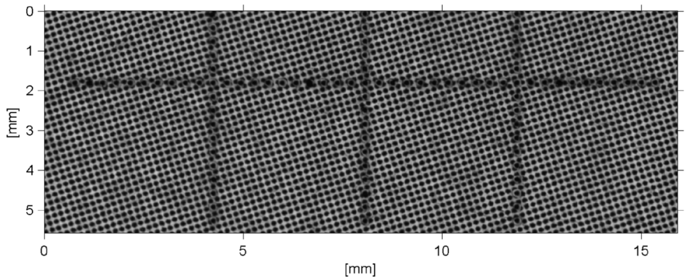

(a) Print reflectance.

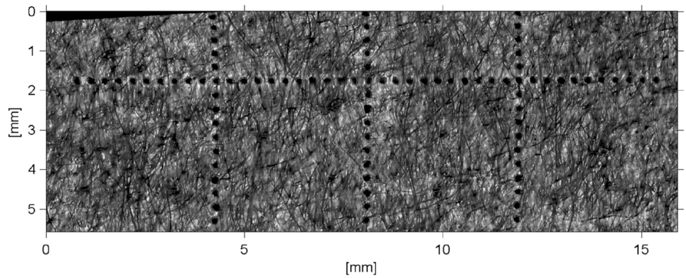

(b) Coating layer thickness.

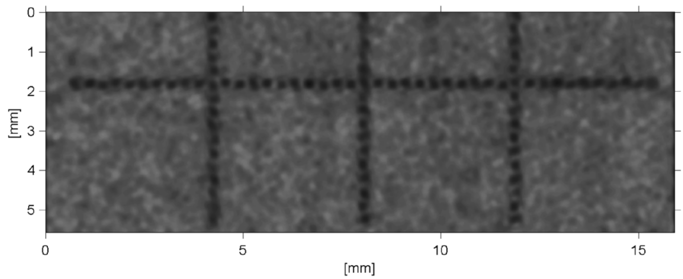

(c) Lowpass filter applied to print reflectance image (a) to remove the dot pattern.

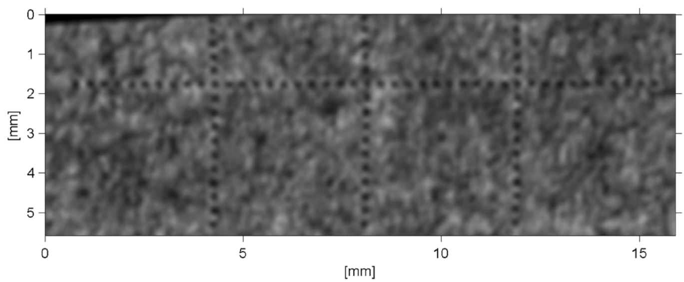

(d) Lowpass filter applied to the coat weight map (b).

Figure 9. Offset printed WFC paper (a) and coating thickness of the same sample (b). Pixel size is $12{\times}12\mu m^2$, values in the coating thickness maps vary from 0 g/m^2 (black) to 30 g/m^2 (white). Low pass filtering is applied to the maps in order to remove the dot pattern from the print (c, d).

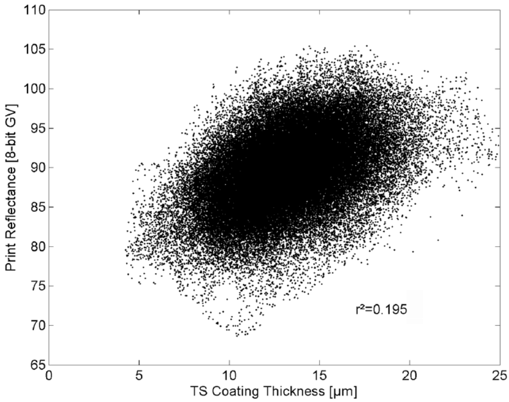

Figure 10. Point-wise linear correlation between coating layer thickness and local print reflectance at a point size of 100*µm*.

Figure 10. Again the linear correlation coefficient is not high, $r^2 = 0.195$. Still, the effect of coat weight variations on local print reflectance is evident.

3.4 Comparing 3D imaging techniques

The proposed method to link 3D and 2D datasets can also be used to combine data from different 3D-imaging techniques. In this case not the actual 3D datasets are connected, instead we link 2D paper property maps generated from 3D data.

In order to illustrate such an application we compare coating layer thickness measurement from light microscopy serial sectioning to measurements from microtomography. A laser marked 90 g/m^2 WFC paper sample was first imaged in an SkyScan 1172 X-ray microtomograph, voxel size was $1.37 \times 1.37 \times 1.37\ \mu m^3$. Subsequent serial sectioning and microscope imaging yielded a resolution of $3 \times 0.81 \mu m^2$ in the paper plane and $0.81 \mu m$ in paper z-direction. Although the pixel size is similar, the slice images of the two methods are very different regarding the appearance of the paper structure, Figure 11. The light microscopic image gives sharp details of the coating layer and the fiber cross sections. The X-ray microtomography images exhibit strong contrast for the coating layer. The coating pigments consist of $CaCO_3$, Calcium has strong absorbancy of X-rays which enhances the contrast of the coating. The tomography image is somewhat blurred, optical resolution of the system is considerably below pixel size. Furthermore there are image artefacts at the paper edges, e.g. the spiderweb-like structures at the bottom side of the laser hole.

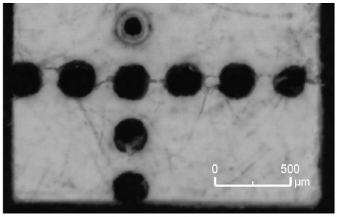

(a)

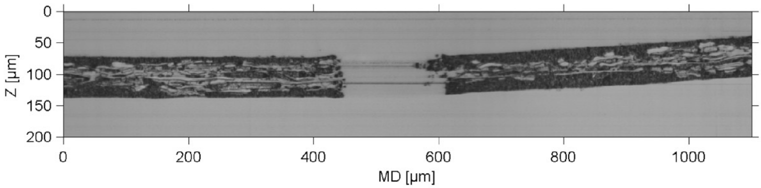

(b) Light microscopy based serial sectioning, pixel size is $0.81\mu m$

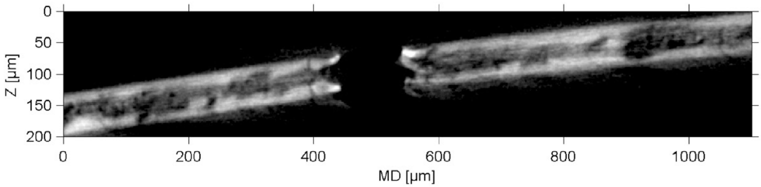

(c) Microtomography, pixel size is $1.37\mu m$.

Figure 11. A wood free coated paper sample with laser marks (a). 3D Imaging slices using light microscopy serial sectioning (b) and microtomography (c). Images (b, c) are taken from *approximately* the same position, the half closed laser hole near the top edge of figure (a).

The coating layer was identified in both 3D datasets, flattened 2D coating layer thickness maps were produced using the previously described method. Although the slice images are looking very different, the results for the local coating thickness were similar, Figure 12. A lot of the small details visible in the serial sectioning result (Figure 12b) are lost in the microtomography measurement (Figure 12a), still most of the large, salient structures appear in both maps.

Again the images have been registered, to compare the results quantitatively using point-wise linear correlation, Figure 12(c). Each point in this figure represents the coating thicknesses on an area of $14 \times 14\mu m^2$. The regions within the dashed lines in Figure 12(a,b) were excluded from the

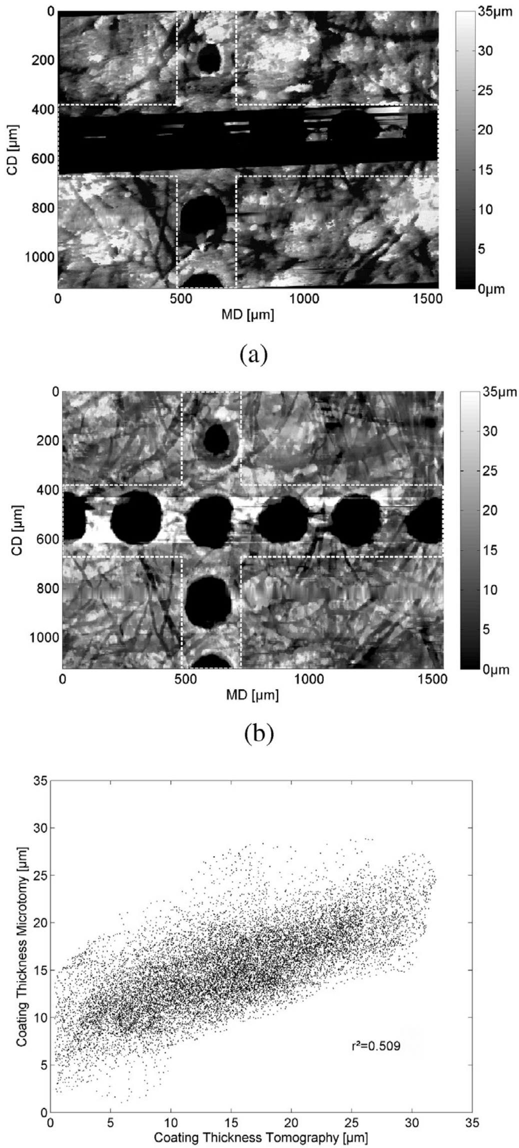

(a)

(b)

(c)

Figure 12. Coating thickness measurement from two different 3D imaging methods, microtomography (a) and light microscopy serial sectioning (b). Point-wise linear correlation (c) between the values in (a) and (b), each point represents an area of $14\times14\mu m^2$.

point-wise correlation because of the laser holes and some measurement artefacts. The absolute values of coating layer thickness are differing considerably between the methods, nevertheless the correlation between the results confirms the visual similarity of the images.

4 CONCLUSIONS AND OUTLOOK

It has been demonstrated, that the introduced concept to link data from 3D paper structure to 2D paper property maps is working and that the accuracy of the procedure is satisfying.

The results regarding the effect of local coating layer thickness on brightness variations and print density variations yielded somewhat lower correlations than expected. Still, we could demonstrate *direct and quantitative* evaluation of the local coating layer structure and its effect on the local print. Linking the optical surface image to the 3D structure of the paper seems to be an interesting method to investigate unevenness of print or paper brightness and how it is affected by coating and calendering.

We believe that the proposed method could open new opportunities for paper structure analysis in both, fundamental and applied research. 3D micro-imaging techniques are developing rapidly in terms of sample size and image quality. Also new and powerful image analysis methods are emerging fast. By enabling a combined analysis of 3-dimensional and 2-dimensional aspects of paper structure, the proposed method might contribute to a better understanding of how paper quality is affected by the interrelation of local paper properties.

5 ACKNOWLEDGEMENTS

We thankfully acknowledge funding of this work by Delfort Group, Mondi, Myllykoski, Norske Skog, Omya, Sappi, SCA, Stora Enso, Voith Paper as well as the Austrian Industrial Research Promotion Agency (FFG).

REFERENCES

1. I. Kajanto. The effect of formation on print quality with woodfree offset papers. *Nordic Pulp and Paper Res. J.*, **4**(1):8–15, 1989.
2. A. Dickson. Evaluating the relationship between grammage, topography and print properties in newsprint. In *60th Appita Annual Conference, Melbourne*, pages 19–23, 2006.

3. M. Mettänen, H. Ihalainen, and R. Ritala. Alignment and statistical analysis of 2-d small scale paper property maps. In *Proceedings of the 2007 International Paper Physics Conference, Gold Coast, Australia*, pages 624–632, 2007.
4. J. Vyörykä, K. Juvonen, D. Bousfield, and T. Vuorinen. Raman microscopy in lateral mapping of chemical and physical composition of paper coating. *Tappi J.*, **3**(9): 19–24, 2004.
5. P. Hansson and P.-A. Johansson. A new method for the simultaneous measurement of surface topography and ink distribution on prints. *Nord. Pulp Paper Res. J.*, **14**(4):315–319, 1999.
6. H. Praast and L. Göttsching. Analyse und Ursachen von Missing Dots im Tiefdruck (in German). *Papier*, **47**(1):12–19, 1993.
7. G. Chinga and K. Syverud. Quantification of paper mass distributions within local picking areas. *Nord. Pulp Paper Res. J.*, **22**(4):441–446, 2007.
8. Y. Sung, C. Ham, O. Kwon, H. Lee, and D. Keller. Applications of thickness and apparent density mapping by laser profilometry. In S. I'Anson, editor, **Trans. XIIIth Fund. Res. Symp.**, volume 2, pages 961–1007, Cambridge, 2005. FRC.
9. J. Pawlak and D. Keller. Relationships between the local sheet structure and z-direction compressive characteristics of paper. *J. Pulp and Paper Sc.*, **30**(9):256–262, 2004.
10. H. Tomimasu, K. Suzuki, and T. Ogura. The effect of basestock structure on coating weight distribution. *Tappi J.*, **73**(5): 179–187, 1990.
11. M. Wiltsche, W. Bauer, and M. Donoser. Coating application method and calendering influence on the spatial coating layer formation obtained by an automated serial sectioning method. In *TAPPI Advanced Coating Fundamentals Symposium*, pages 413–425, 2006.
12. K. Peiponen, E. Alarousu, M. Juuti, and R. Myllyla. Diffractive-optical-element based glossmeter and low coherence interferometer in assessment of loacal surface quality of paper. *Optical Eng.*, **45**(4):043601.1–043601.7, 2006.
13. P. Mangin, M.-C. Béland, and L. Cormier. A structural approach to paper surface compressibility – relationships with printing. In C.F. Baker, editor, **Trans. Xth Fund. Res. Symp.**, pages 1397–1427, Oxford, 1993. FRC.
14. B. Drouin, R. Gagnon, A. Schroeder, J. Silvy, and M. Butel. High-resolution fibre orientation and basis weight measurement. *J. Pulp and Paper Sc.*, **22**(7):J237–J241, 1996.
15. S. Rolland du Roscoat, X. Thibault, and J.-F. Bloch. Characterisation of the 3D paper structure with x-ray synchrotron radiation microtomography. In S.J. I'Anson, editor, **Trans. 13th Fund. Res. Symp.**, pages 901–920, 2005.
16. C. Antoine, P. Nygard, O. Gregersen, R. Holmstad, T. Weitkamp, and C. Rau. 3D images of paper obtained by phase contrast x-ray microtomography: image quality and binarisation. *Nuclear Instruments and Methods in Physics Research A*, **490**:392–402, 2002.
17. A. Sasov, F. Nadeem, X. Liu, and K. Verelst. Adaptive acquisition geometry for micro-ct with large format detectors. In *Proceedings of SPIE*, volume 7078, page Art. no. 70781Q, 2008.

18. E. Alarousu, L. Krehut, T. Prykri, and R. Myllyla. Study on the use of optical coherence tomography in measurements of paper properties. *Measuremet Science and Technology*, **16**:1131–1137, 2005.
19. M. Wiltsche, M. Donoser, W. Bauer, and H. Bischof. A New Slice-Based Concept for 3D Paper Structure Analysis Applied to Spatial Coating Layer Formation. In S.J. I'Anson, editor, **Trans. 13th Fund. Res. Symp.**, pages 853–899, 2005.
20. I. Sintorn, S. Svensson, M. Axelsson, and G. Borgefors. Segmentation of individual pores in 3d paper images. *Nordic Pulp and Paper Res. J.*, **20**(3):316–319, 2005.
21. B. Lozo, J. Vyörykä, T. Vuorinen, and T. Muck. Nondestructive micrscopic and spectroscopic methods for depth profiling of ink jet prints. *J Imaging Science and Technology*, **50**(4):333–340, 2006.
22. M. Aronsson. Estimating fibre twist and aspect ratios in 3d voxel volumes. In *16th International Conference on Pattern Recognition, Proceedings.*, volume 1, pages 218–221, 2002.
23. M. Juuti, T. Prykri, E. Alarousu, H. Koivula, M. Myllys, A. Läntelä, M. Toivakka, J. Timonen, Risto MYllyl, and K.-E. Peiponen. Detection of local specular gloss and surface roughness from black prints. *J. Imaging Science and Technology*, Colloids and Surfaces A: Physiochem. and Engineering Aspects: 101–108, 2008.
24. P. Vernhes, S. Rolland du Roscoat, A. Blayo, B. Pineaux, X. Thibault, and J.-F. Bloch. Synchrotron x-ray microtomography: A new tool to characterize the interaction between paper and toner. *J. Imaging Science and Technology*, **52**(l):010502.1–010502.6, 2008.
25. U. Hirn, M. Lechthaler, and W. Bauer. Registration and correlation of local paper property maps. *Nordic Pulp and Paper Res. J.*, **23**(4):374–381, 2008.
26. R. Brockmann. Laserperforation ermöglicht bis zu 30.000 Mikrobohrungen pro Sekunde. *Das Papier*, **53**(2): 101–109, 1999.
27. E. Bessonov, M. Dvernitsky, V. Emelianov, V. Kravchenko, Y. Sdobnikov, and A. Skorbun. The laser perforator of passports. In V. Veiko, editor, *Laser-Assisted Microtechnology* 2000, volume 4175, pages 124–128, 2001.
28. N. Lange, S. Meissner, and M. Walter. Method and apparatus for perforating cigarette paper and the like. In *US Patent 5259401*, 1992.
29. M. Beleastro, L. Duvekot, K. Rudolph, and M. Thompson. High speed laser perforation of cigarette tipping paper. In *United States Patent 7393313*, 2006.
30. John F. Ready. Applications of material removal: Drilling, cutting, marking (chapter 16). In *Industrial Applications of Lasers*, pages 384–418. Academic Press, 1997.
31. M. Pilu. Undoing curl distortions using applicable surfaces. In *Proceedings of the IEEE Conference on Computer Vision and Pattern Recognition*, volume 1, pages 167–172, 2001.
32. W. Liang and H. Bin. Optimal flattening of freeform surfaces based on energy model. *Int. J. Manufactoring Technology*, **24**:853–859, 2004.
33. M. Brown and B. Seales. Image restoration of arbitrarily warped documents.

IEEE Transactions on Pattern Analysis and Machine Intelligence, **26**(10):1295–1306, 2004.

34. K.-B. Chua, L. Zhang, Y. Zhang, and C.-L. Tan. A fast and stable appproach for restauration of warped documents. In *IEEE International Conference on Document Analysis and Recognition*, pages 384–388, 2005.
35. M. Sun, R. Yang, L. Yun, G. Landon, B. Seales, and M. Brown. Geometric and photometric restoration of distorted documents. In *Proc. of the 10th IEEE Conference on Computer Vision*, 2005. DOI 10.1109/ICCV.2005.237.
36. W. Press, S. Teutolsky, W. Vetterling, and B. Flannery. **Numerical Recipes in C**, chapter 16, Integration of ordinary differential equations, pages 707–722. Cambridge University Press, 1992.
37. W. Hauger, W. Schnell, and D.Gross. **Technische Mechanik – Band 3 – Kinetik**. Springer, 4th edition, 1993.
38. C.B. Barber, D.P. Dobkin, and H.T. Huhdanpaa. The quickhull algorithm for convex hulls. In *ACM Transactions on Mathematical Software*, volume 22, pages 469–483, 1996.
39. L. Gottesfeld Brown. A survey of image registration techniques. *ACM Computing Surveys*, **24**(4):325–375, 1992.
40. B. Zitova and J. Flusser. Image registration methods: A survey. *Image and Vision Computing*, **21**:977–1000, 2003.
41. M. Petrou. Image registration: An overview. *Adv. Imaging and Electron Physics*, **130**:243–291, 2004.
42. M. Wanske, H. Großmann, and S. Scherer. Messtechnische Bewertung von Tissue Produkten mit dem optischen Messsystem InfiniteFocus. *Wochenblatt der Papier-fabrikation*, **136**(9):473–477, 2008.
43. M. Leskkelä. **Paper Physics**, volume 16 of *Papermaking Science and Technology*, chapter 4 – Optical Properties, pages 117–137. Fapet Oy, 1998. ISBN 952-5216-16-0.
44. M. Larsson, D. Vidal, G. Engström, P. Lepoutre, and X. Zhou. Paper coating properties as affected by pigment blending and calendering – an experimental study. In *22nd PTS Coating Symposium, Munich*, pages 24.1–24.16, 2005.
45. J. Vyörykä, K. Juvonen, D. Bousfield, and T. Vuorinen. Raman microspectroscopy in the lateral mapping of paper coating composition. In *TAPPI Coating Conference*, 2002.

Transcription of Discussion

INTRODUCING A CONCEPT TO LINK 3D PAPER STRUCTURE TO 2D PAPER PROPERTIES

Ulrich Hirn,[1] *Johannes Kritzinger*,[1] *Michael Donoser*[2] and *Wolfgang Bauer*[1]

[1]Institute for Pulp, Paper and Fiber Technology, Graz University of Technology, Austria
[2]Institute for Computer Graphics and Vision, Graz University of Technology, Austria

Ilya Vadeiko FPInnovations

I have two questions, but fairly short ones. First, when you match 2D patterns after flattening, do you allow just rotational and translational transformations or can you also stretch/contract one of the two patterns?

Ulrich Hirn

We use translation and rotation transformations plus rescaling, but we have no nonlinear deformation yet. But of course, it would be interesting to the same type of grid to also be able to perform nonlinear de-skewing.

Ilya Vadeiko

And the second question, you showed the correlation between two different images that you acquired with different methods. Have you tested these correlations before and after applying the whole procedure that you have developed? Does the procedure of matching two patterns improve the correlation? Maybe at this scale it is not making any big difference.

Discussion

Ulrich Hirn

What we did is that first we have this 3D data set, and we have some 2D measurements, or we have another 3D data set. We did not make any direct comparison between them because we would have needed some three-dimensional registration procedure.

Ilya Vadeiko

Yes, but I mean after you project your three-dimensional structure onto a plane, but before you do the compensation based on your springs algorithm.

Ulrich Hirn

Yes, now I understand. This is definitely a large improvement because, as you can see here (refers to figure 4 in the paper in the proceedings, ed.), this plane is curved and tilted so this region of the plane is severely compressed when directly mapped to a planar structure. So it really needs to expand here for maybe 200 or 300 µm so that you really can match the structures. So to answer your questions, yes it does bring a substantial improvement, but I have no graph of this here.

Ilya Vadeiko

I was wondering because, when you look at the map of points that you showed for the correlation, it is a fairly spread cloud of points. So my guess was that maybe the procedure is not giving a great improvement at those levels, where correlation is perhaps 50% or even 20%.

Ulrich Hirn

Well, maybe it is, when you do it straightforwardly it would be 0.08 or something like that, as a rough indication. After correction it is 0.19.

Ilya Vadeiko

Thank you.

Roger Gaudreault Cascades R&D

I have a follow-up question. In your minimization procedure for the modelling video, you had a convergence parameter which is less than 0.1. Is this parameter distance-based or energy-based or do you use another technique?

Ulrich Hirn

This is for size and geometry, so we measure the actual size which is in x and y directions, and the geometry which is the shear distortion and the degree of parallelness between the surfaces. So I think it covers all relevant aspects of deformation.

Roger Gaudreault

But, do you use first derivatives or second derivatives when you do the minimization?

Ulrich Hirn

It is just a model. What we actually have is the spring forces, and then we set up Newton's Law and state that mass × acceleration is the sum of the forces and by that we define the movement. I know that there are other approaches to relax the mesh – like direct energy minimization approaches – that are also applicable to this type of problem.

Roger Gaudreault

Yes, in molecular mechanics, for example, we minimize with energy. We use second derivative to ensure we find the global minima.

Ulrich Hirn

If you do direct displacement of the node without having a velocity to determine the whole thing, convergence becomes very slow towards the end, so this is why we chose this approach.

Ramin Farnood University of Toronto

Thank you for an interesting presentation. I have a comment and a question. My comment is regarding the method that you used for coating weight or coating thickness distribution. Obviously, microtomy and tomography can provide a lot of information, but if you are only interested in coating non-uniformity at a small scale, there are perhaps easier ways. For instance, we have published a paper, which came out in JPPS just recently, in which we used X-ray transmission and mapped the coating weight distribution, which is much easier than this technique. So if you are interested in that, I think that is probably a better way of doing it. My question is regarding the comparison that you made between your printed image and coating thickness distribution. Specifically I was curious to know if you have done any cross-correlation between these images?

Ulrich Hirn

Yes, we did it here (refers to figure 10 in the paper in the proceedings, ed.). So this is the cross-correlation $r^2 = 0.2$, or 20% of the variance in print reflectance is explained by coating layer thickness variations.

Tetsu Uesaka FPInnovations

This is very much a procedure question. You can easily determine the centre line, or centre plane, for small sample but if you push for a larger size, you may have very large distortion, right? So the question is, does this procedure work well for much larger samples? I guess it is really the objective.

Ulrich Hirn

The whole procedure is only necessary if you have larger samples because then, during 3D imaging, these deformations occur. If you have smaller samples, they are flat, so you could directly convert them to 2D maps. The main motivation of the whole thing was that we saw that the larger 3D maps had these curves and deformations.

Tetsu Uesaka

How large can the samples be? What you are using right now is relatively small – about 1.5 mm.

Ulrich Hirn

The maximum size is around 15–20 mm with something like 10 µm in-plane resolution and about 0.9 µm in the paper thickness directions. I think this is about what we can do now; we cannot get any larger yet.

Tetsu Uesaka

Thank you.